Soft Matter

Accepted Manuscript

This article can be cited before page numbers have been issued, to do this please use: S. He, Z. Chang, D. Liang, C. Li, Q. Liang, X. Yin and G. Xu, *Soft Matter*, 2025, DOI: 10.1039/D5SM00380F.

ROYAL SOCIETY OF CHEMISTRY

rsc.li/soft-matter-journal

View Article Online
DOI: 10.1039/D5SM00380F

Self-enhanced mobility mechanism drives the spontaneous emergence and transformation of vortex patterns

Shuang-Quan He [a,b], Zhuo Chang [a,b], Dong Liang [a], Chen-He Li [a], Qian-Lei Liang [c], Xu Yin [d,*] and Guang-Kui Xu [a,b*]

a. *Laboratory for Multiscale Mechanics and Medical Science, Department of Engineering Mechanics, State Key Laboratory for Strength and Vibration of Mechanical Structures, School of Aerospace Engineering, Xi'an Jiaotong University, Xi'an 710049, China*
b. *Medical Device Interdisciplinary Mechanics and Health Diagnosis Center, Chengxing Guotou & Xi'an Jiaotong University Union Laboratory, Taizhou 225400, China*
c. *Department of Neurosurgery, China-Japan Union Hospital of Jilin University, Changchun 130000, China*
d. *Institute of Biomechanics and Medical Engineering, Applied Mechanics Laboratory, Department of Engineering Mechanics, Tsinghua University, Beijing 100084, China*

Abstract

Active systems frequently exhibit remarkable self-organization phenomena, characterized by transition from disorder to order. Yet, the underlying mechanisms driving the spontaneous emergence and transformation of vortex patterns within these systems remain poorly understood. In this study, we introduce a chiral self-propelled rod (CSPR) model that integrates a self-enhanced mobility mechanism, wherein the propulsion speed of individual particles is positively regulated by the local alignment and density of their neighbors. Using this model, we successfully reproduce a wide spectrum of vortex self-organization behaviors in chiral active systems. Our findings reveal that the self-enhanced mobility mechanism plays a pivotal role in driving the spontaneous formation of vortices and mediating the transitions between distinct vortex patterns by modulating their size and number. Furthermore, we identify a non-monotonic dependence of the system mean velocity and vorticity on the aspect ratio of the rods, with an optimal aspect ratio that maximizes both quantities. Finally, through an analysis employing three correlation functions, we demonstrate that variations in both self-enhanced mobility and aspect ratio markedly affect the angular and spatial correlations within vortex structures. These simulation results align well

*Correspondence to: yinxu6252@163.com (X. Yin) or guangkuixu@xjtu.edu.cn (G. K. Xu).

with experimental observations, offering theoretical insights to bridge collective dynamics of active microswarms with practical applications in bio-inspired microrobotic systems.

Keywords: Active matter; Self-enhanced mobility; Chiral self-propelled rod model; Vortex pattern transformation; Correlation function

View Article Online
DOI: 10.1039/D5SM00380F

1 Introduction

Active matter consists of living or synthetic units that convert locally supplied free energy into mechanical work, inherently existing in a non-equilibrium state [1, 2]. This unique energy conversion mechanism enables active matter to exhibit a diverse range of self-organization phenomena, such as active vortices [3, 4], mesoscale turbulence [5, 6], topological defects [7, 8], and motility-induced phase separation [9-11]. Among these phenomena, vortex motion is ubiquitous across various scales in nature, ranging from the vortex state of microactive particles [12, 13] to the flocking behavior of animals [14, 15], and then even extending to large-scale atmospheric cyclones [16]. Further studies reveal that such vortical patterns, mediated by long-range spatial correlations, play a central regulatory role in key biological processes, including cell migration [17], signal transmission [18], and ecological interaction [19]. Furthermore, biomimetic insights derived from active particle studies not only enhance our understanding of living systems but also drive innovative design strategies for self-assembled dynamic materials [20, 21] , and microrobotics [22]. Therefore, revealing this complexity formation mechanism driving the emergence of self-organizing phenomena, including rotation and vortex motion, is a critical frontier in both nonequilibrium physics and bioengineering innovation.

To elucidate the underlying mechanisms of spontaneous vortex formation, a number of efforts have been directed from different perspectives. Recent experiments have revealed that mechanical flexibility and intrinsic chiral motion of *Plasmodium* can result in self-organized vortex patterns during collective movement [23] (see Figure 1(a1)). Sumino et al. [13] and Nakane et al. [24] quantitatively studied the key effects of

View Article Online
DOI: 10.1039/D5SM00380F

differences in physical density distribution (see Figure 1(a2)) and chemical nutrient concentration (see Figure 1(a3)) in vortex emergence. These spatiotemporal organizations are driven by the presence of the synergistic effects between individuals and the chemotaxis effects, respectively. Furthermore, a series of experiments focused on the movement patterns of swimming bacteria in confined environments, which spontaneously form spiral vortices in thin cylindrical chambers [25-27] (see Figure 1(a4)). Up to now, much is known about the generation and transformation of vortices through artificial experimental conditions, such as shape features, boundary constraints, and concentration differences. However, more recently, Xu et al. found that dense bacterial suspensions can spontaneously develop a lattice of mesoscale, fast-spinning vortices [28]. Despite these advances, the field currently lacks a unified theoretical framework capable of predicting the spontaneous emergence and dynamic evolution of large-scale vortex states in dense active matter systems.

From a theoretical standpoint, phenomenological approaches have proven to be powerful in addressing the complex many-body problems inherent to active matter systems. These methods enable the systematic coarse-graining of microscopic details into macroscopic continuum descriptions while preserving essential physical features. Classical frameworks such as Vicsek-type models [29-32] and active Brownian particle models [33-35] have successfully captured emergent collective behaviors through minimal representations of particle dynamics. Increasing evidence suggests that individual particle characteristics, particularly shape anisotropy and mechanical properties, play a crucial role in determining large-scale collective dynamics [23]. This recognition has

View Article Online
DOI: 10.1039/D5SM00380F

motivated the development of self-propelled rod (SPR) models [36-39] , which explicitly incorporate morphological parameters into the theoretical framework. Such models provide a more comprehensive platform for investigating how particle-level heterogeneities affect system-wide self-organization phenomena. Notably, SPR models have demonstrated remarkable success in both qualitatively reproducing and quantitatively explaining complex self-organization patterns observed in experiments through well-defined mechanical and physical parameters [40-42]. This theoretical progress has significantly enhanced our ability to bridge microscopic interactions with macroscopic emergent phenomena in active matter systems.

Here, we propose a chiral self-propelled rod model that embeds the self-enhanced mobility mechanism, enabling systematic investigation of autonomous patterning phenomena in both dense living systems and synthetic active matter. Through extensive numerical simulations, we demonstrate that this model naturally captures the emergence of stable vortex patterns observed in experimental systems. Our study reveals the non-monotonic dependence of the mean velocity and vorticity of the system on the aspect ratio of the rods, with both quantities reaching their maxima at an optimal aspect ratio. These findings align well with experimental observations, confirming that morphological heterogeneity at the individual level plays a crucial role in governing collective behavior. Importantly, we identify that the transition between different vortex regimes is mediated by the self-enhanced mobility mechanism, which modulates both the characteristic vortex size and their spatial distribution. To quantitatively characterize these effects, we employ three distinct correlation function

View Article Online
DOI: 10.1039/D5SM00380F

analyses. These results provide new insights into how microswimmers morphology and self-enhanced mobility collectively affect the emergent dynamics of self-propelled systems.

2 Model

Here, we develop a biomechanical model to investigate spontaneous multivortex states in an open chiral self-propelled system, as shown in Figure 1(b)-(d). The potential energy of the system is contributed by the interaction among self-propelled rods. Each rod is divided into n equidistant segments, resembling spheres with a diameter *d*. The interaction between any two segments from different rods is governed by a Yukawa potential [43]. The pair potential of two rods α and β, characterized by orientation vector $\left(\boldsymbol{u}_\alpha, \boldsymbol{u}_\beta\right)$ and center distance $\Delta \boldsymbol{r}_{\alpha\beta}$, is given by

$$E_{\alpha\beta} = \frac{E_0}{n^2} \sum_{i=1}^{n} \sum_{j=1}^{n} \frac{\exp\left[-\left(r_{ij}^{\alpha\beta}/\lambda\right)\right]}{r_{ij}^{\alpha\beta}}, \tag{1}$$

where E_0 is the Yukawa potential amplitude, λ represents the screening length, and

$$r_{ij}^{\alpha\beta} = \left|\Delta \boldsymbol{r}^{\alpha\beta} + \left(l_i \boldsymbol{u}^{\alpha} - l_j \boldsymbol{u}^{\beta}\right)\right|, \tag{2}$$

denotes the distance between the *i*-th segment of the rod α and the *j*-th segment of the rod β, with $i, j = \ldots, n$; $l_i \in \left[-\left(l-\lambda\right)/2,\ \left(l-\lambda\right)/2\right]$ being the position of the segment i along the symmetry axis of the rod α. Finally, the potential energy of the system is summarized as [44]

$$E = \frac{1}{2} \sum\nolimits_{\beta,\alpha:\beta\neq\alpha} E_{\alpha\beta}, \tag{3}$$

We consider a system of *N* active rods that extract energy from the environment to sustain their self-propelled motion. Their dynamics can be determined by the

View Article Online
DOI: 10.1039/D5SM00380F

evolutions of the center-of-mass $\{\boldsymbol{r}_\alpha(t)\} = \{(x_\alpha(t), y_\alpha(t))\}$ and the orientation $\boldsymbol{u}_\alpha = (\cos\theta_\alpha, \sin\theta_\alpha)$ of each rod α, which obey the overdamped Langevin dynamics:

$$\frac{\mathrm{d}\boldsymbol{r}_\alpha}{\mathrm{d}t} = \boldsymbol{f}_{\mathrm{T}}^{-1} \cdot \left(\mathbf{F}_\alpha^{\mathrm{A}} - \mathbf{F}_\alpha^{\mathrm{P}}\right), \tag{4}$$

$$\frac{\mathrm{d}\theta_\alpha}{\mathrm{d}t} = f_{\mathrm{R}}^{-1} \cdot \left(-\frac{\partial E}{\partial \theta_\alpha}\right) + \omega_\alpha + \frac{\mu_\theta}{N_\alpha} \sum_{\kappa \in R_\alpha} \sin(\theta_\kappa - \theta_\alpha) + \zeta_\theta, \tag{5}$$

$$\frac{\mathrm{d}\omega_\alpha}{\mathrm{d}t} = -\frac{\omega_\alpha}{\xi} + \frac{\mu_\omega}{N_\alpha} \sum_{\kappa \in R_\alpha} (\omega_\kappa - \omega_\alpha) + \zeta_\omega + \zeta_{\mathrm{bias}}, \tag{6}$$

where $\boldsymbol{f}_{\mathrm{T}}$ denotes the translational friction tensor, f_R represents the rotational friction constant (see section S1 in the Supporting Information for details), and ξ is relaxation time. In Eqs.(4)-Eq.(6), the dot represents a temporal derivative.

In Eq. (4), the active motile force on the α-th rod is described as

$$\mathbf{F}_\alpha^{\mathrm{A}} = F_\alpha \boldsymbol{u}_\alpha, \tag{7}$$

F_α denotes the self-propulsion force derived from ambient energy. The dynamic of the α-th rod, driven by its self-propulsion force, is governed by the equation (Figure. 1(d)):

$$F_\alpha = \mu_\alpha f_\alpha, \tag{8}$$

where μ_α represents variable mobility of the self-propelled rod α, and f_α denote the self-propulsion force. For each self-propelled rod, the self-propulsion force f_α is sampled from a Gaussian distribution with a mean of f_0 and a standard deviation of $0.4 f_0$, capturing the heterogeneity of cell motility [28]. Self-enhanced motility emerges as a universal paradigm regulating autonomous patterning phenomena in dense living systems and synthetic active matter [45]. Many experiments showed that the regions of high orientational order in the bacterial suspensions have locally high swimming

velocity, while orientationally disordered regions have lower velocity [46, 47]. The positive correlation between the distribution of swimming velocity and the orientation order implies the self-enhanced mobility mechanism of active systems. Subsequently, Xu et al. provided further specific linear relation based on the experimental results of single-cell velocity measurement and named this positive correlation as the self-enhanced mobility mechanism [28]. This mechanism realizes variable mobility of individual chiral rods through internally generated local collective active stress (derived from higher polar order of cellular motion) [48]. In our model, the variable mobility μ_α as a specific manifestation of a self-enhanced mobility mechanism, and follows a linear relation with the local polar order in the vicinity of self-propelled rod α. This relationship is expressed as follows [28]

$$\mu_\alpha = \Gamma_0 \left(1 + \beta_e P_\alpha\right), \tag{9}$$

here $\beta_e \geq 0$ denotes the dimensionless mobility enhancement coefficient, Γ_0 denotes the density correlation coefficient, P_α represents the local polar order near the self-propelled rod α, and is calculated by

$$P_\alpha = \left\langle \left| \sum\nolimits_j \frac{\mathrm{d}\boldsymbol{r}_j / \mathrm{d}t}{\left|\mathrm{d}\boldsymbol{r}_j / \mathrm{d}t\right|} \middle/ m_\alpha \right| \right\rangle_{t_0}, \tag{10}$$

where the summation is taken over m_α rods within the neighbourhood of rod α (with $\left|\mathbf{r}_j - \mathbf{r}_\alpha\right| \leq 1$; including self-propelled rod α itself), with the angular bracket denoting averaging over time to reduce fluctuations. The key parameters in self-enhanced mobility mechanism are listed in Table. 1.

Table. 1. Parameter description of self-enhanced mobility mechanism

Parameter	Description	Reference

View Article Online
DOI: 10.1039/D5SM00380F

β_e	Mobility enhancement coefficient	28
P_α	Local polar order near the α-th chiral rod	28
μ_α	Variable mobility of α-th chiral rod	28
Γ_0	A constant parameter depends on local density	28

In the equation (Eq.(4)), the absence of torques between rods implies that their interaction is governed solely by the passive force

$$\mathbf{F}_\alpha^{\mathrm{P}} = -\nabla_{\boldsymbol{r}_\alpha} E\,, \tag{11}$$

$\boldsymbol{u}_\alpha = (\cos\theta_\alpha, \sin\theta_\alpha)$ is a unit vector along the long axis of the rod, representing its polarity. In this study, we incorporate two social interactions between neighboring active particles (μ_θ and μ_ω), along with their internal processes, which originate from mechanical contact-induced quorum sensing [49]. Firstly, μ_θ in Eq. (5) denotes the strength of polarization alignment between velocity directions, arising from steric and hydrodynamic interactions between rods. The second type of interaction involves diffusive coupling of angular velocities due to local fluid vorticity, characterized by angular velocity alignment strength μ_ω in Eq. (6). Here, N_α refers to the number of neighborhood rods of the α-th rod, and $\sum_{\kappa\in R_\alpha}$ computes a summation over all neighboring rods of rod α within the perception radius *R*.

In Eqs. (5) and (6), ω_α is angular velocity of the rod α. The chirality term ω_α allows the synchronization of local rotational motion, arising from short-time memory effects of local fluid vorticity. Note that the chirality term ω_α implicitly defines Eq.(5) as a chiral self-propulsion rod model. τ being relaxation time. Finally, to account for random fluctuations in the microenvironment, Gaussian white noises ζ_θ and ζ_ω are introduced

View Article Online
DOI: 10.1039/D5SM00380F

$$\left\langle \zeta_a^{\theta}(t)\zeta_b^{\theta}(t')\right\rangle = \gamma_{\theta}^2\delta(t-t')\delta_{ab}, \tag{12}$$

$$\left\langle \zeta_a^{\omega}(t)\zeta_b^{\omega}(t')\right\rangle = \gamma_{\omega}^2\delta(t-t')\delta_{ab}, \tag{13}$$

where γ_{θ} and γ_{ω} represents the magnitude of the fluctuation, and δ_{ab} and $\delta(t-t')$ are the Kronecker delta and Dirac delta functions, respectively. Furthermore, the 'bias' noise raises the intriguing possibility that it, along with diffusive coupling between angular velocities, may contribute to chiral symmetry breaking. It is written as [50]

$$\zeta_{\text{bias}} = \text{sign}(\omega_{\alpha})\exp\left(-\frac{|\omega_{\alpha}|}{\omega_0}\right)\zeta, \tag{14}$$

where ζ being a uniform noise in $[0,\eta_{\text{bias}}]$, and the 'bias' noise is aligned with the current sign of the angular velocity and its amplitude decreases with the absolute value of the angular velocity. During the process of dynamic evolution, the changes in the magnitude and direction of the angular velocity of individual chiral rods result from the co-regulation of the diffusive coupling of angular velocities from surrounding chiral rods and small disturbances of white noise. Therefore, the sign of angular velocity is spontaneously generated, and system chirality induced by 'bias' noise is also generated autonomously. These two types of noise lead to a spatially homogeneous and globally oscillating velocity field.

By solving the above governing equations (Eqs. (1)-(14)), one can obtain a non-equilibrium vortex state of chiral self-propelled rods. For simplicity but without loss of generality, we normalize the system by using the length scale *d*, time scale τ, and force scale *F*. In the simulations, we randomly distribute 10000 rods ($N=10000$) within a square box ($L=30$) with periodic boundaries. Other parameters can be

View Article Online
DOI: 10.1039/D5SM00380F

readily normalized: $l = 2.5$, $d = 1.0$, $R = 5$, $\xi = 1.5$, $\Gamma_0 = 1$, $\mu_\theta = 0.4$, $\mu_\omega = 2.0$, $\omega_0 = 5$, $\gamma_\theta = 0.02$, $\gamma_\omega = 0.02$ and $\eta_{\text{bias}} = 1$. Note that all parameters except variables under study are the same as these parameters.

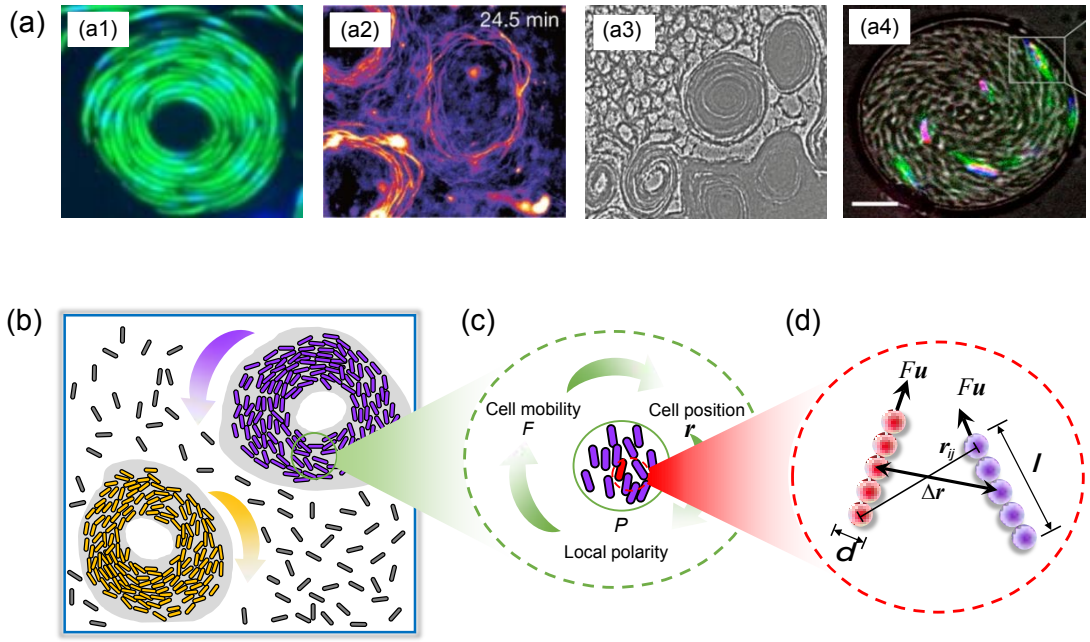

Fig. 1. Illustration of the chiral self-propelled rod model of collective microswimmers. (a) Vortex phenomena have been widely observed in (a1) collective migration of malaria parasites [23], (a2) emergence of vortices of microtubules [13], (a3) collective motion of Gliding *Flavobacteria* [24] and (a4) swimming bacteria in confined suspensions [26]. (b) Schematic of a pair of chiral vortex of self-propelled rod system in a two-dimensional region. (c) Self-enhanced mobility mechanism feedback loop: the movement induction position of microswimmers changes, and then the polarity of local areas regulates the movement of individual microswimmers. (d) Schematic of the self-propulsion force F acting along the main rod axis indicated by the orientational unit vector.

3 Results

3.1 Spontaneous Vortex Formation in Chiral Self-propelled System

3.1.1 Status description of Chiral self-propelled system

We first investigate the collective behavior of a chiral self-propelled rod system with a self-enhanced mobility mechanism. As shown in Figure 2(a), we observe that the system initially exhibits a disordered state, progresses through a transitional phase, and ultimately stabilizes into a well-defined vortex structure. At the global scale, the

View Article Online
DOI: 10.1039/D5SM00380F

establishment of stable vortex rings induces pronounced spatial heterogeneities in both density and vorticity fields. To quantitatively characterize these rotational patterns, we compute the two-dimensional vorticity field $\omega = \nabla \times \mathbf{v}$. i.e., $\omega = \partial_x v_y - \partial_y v_x$ with $v_z = 0$ in two-dimensions [51]. This metric provides a rigorous measure of local swirling motions within the cellular collective. For the convenience of analysis, we evaluate the mean vorticity of the vortex ring through spatially resolved measurements. Six reference points (A-F) are uniformly selected within the angular range ($\pi/3$, 2π), radially centered on the vortex centroid. The spatial average of vorticity magnitudes at these positions yields the representative vorticity value for the vortex ring, as presented in Figure 2(b).

In addition, in order to quantitatively understand the collective motion of chiral self-propelled rods, we introduce an indicator: the angular order parameter, which characterizes the circumferential 'space-phase order' within the system. This angular order parameter is written as [52, 53]

$$S_{\pm} = \frac{1}{N}\sum_{\alpha=1}^{N} e^{i(\phi_\alpha \pm \theta_\alpha)} \tag{15}$$

where, $\phi_\alpha = \tan^{-1}\left(y_\alpha / x_\alpha\right)$, and ϕ_α is the angular position of a chiral self-propelled rod α with respect to the vortex centroid, corresponding to the azimuthal angle. Here, the spatial coordinate determination of the vortex centroid is based on the velocity circulation; x_α and y_α are the spatial coordinate of the rod relative to the vortex centroid; And θ_α is the angle between the α-th rod and the *x*-axis. The angular order parameter *S* quantifies the correlation between the rods' spatial arrangement and their orientations. When there is no correlation between the angular position and orientation

View Article Online
DOI: 10.1039/D5SM00380F

angle, $S_{\pm}=0$; Conversely, when the correlation is maximal, $S_{\pm}=1$. Throughout our simulations, we consider the steady-state value of S, defined as its maximum attained value (S_{+},S_{-}) after the system reaches dynamic equilibrium.

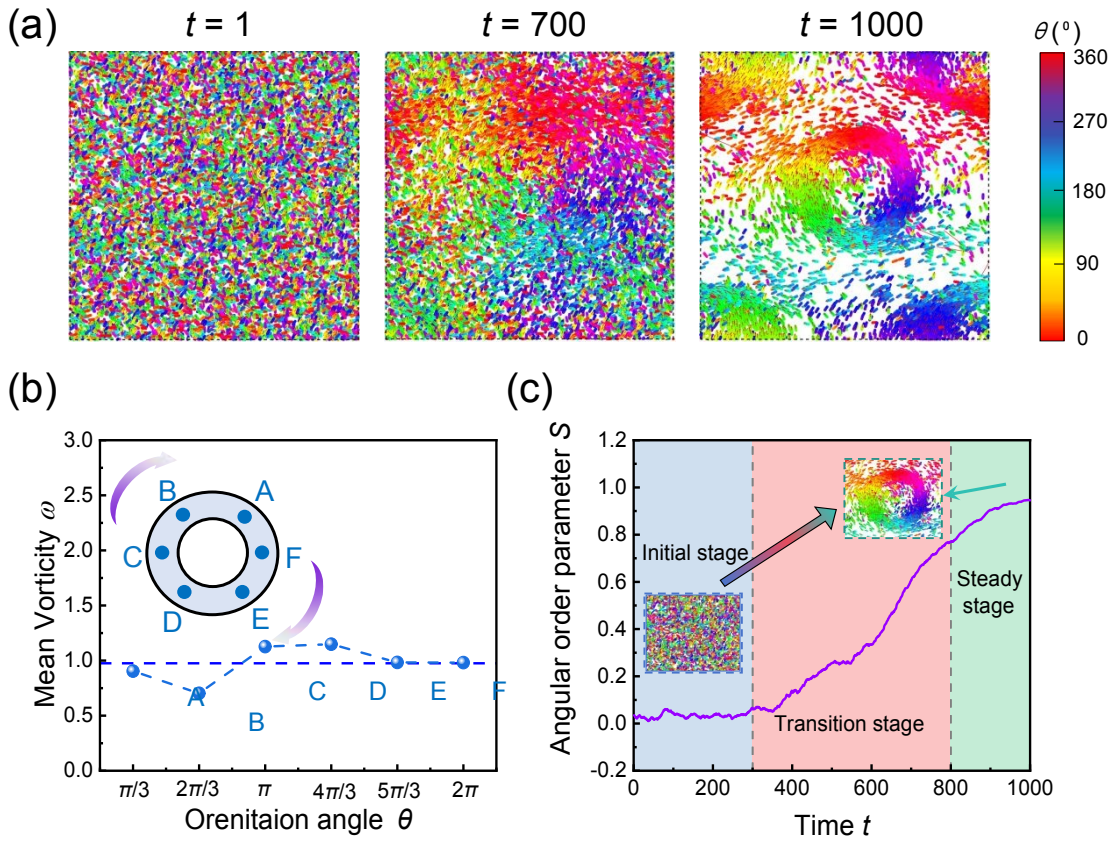

Fig. 2. Description of the dynamic evolution process of spontaneous vortex phenomena. (a) Snapshots of chiral self-propelled rods during time evolution. (b) Schematic diagram of average vorticity calculation. (c) Variation of the angular order parameter S of chiral self-propelled rod system with respect to the simulation time t.

Figure 2(c) illustrates the evolution of the angular order parameter S over time in the chiral self-propelled rod system. The progression of S allows us to categorize the spontaneous vortex formation process into three well-defined dynamical stages. In the initial stage, S fluctuates randomly at low values, signaling the initially uncorrelated distribution of rod orientations and positions. In the transition stage, S exhibits a linear increase, reflecting the system's progressive organization. Finally, in the steady-state stage, S approaches to be 1, indicating the establishment of a stable vortex structure.

View Article Online
DOI: 10.1039/D5SM00380F

Indeed, the numerical variation of angular order parameter S profoundly reflects the characteristics of chiral systems at different stages. During the dynamic evolution process, spontaneous fluctuations of the self-propelled rod system could give rise to regions with higher polar order (and hence with higher collective stress); such regions, with higher velocity and longer persistence time than less-ordered regions, could recruit nearby chiral rods via polar alignment interactions and grow in size until chiral rods recruitment is dynamic balanced by chiral rods loss, eventually developing into stable vortices (i.e., $S \approx 1$). Thereby, the variation of the local region polarity and the mean velocity of the chiral rods contribute to the generation of the vortex structure and indirectly regulate the steady-state pattern of stable vortices. This evolution arises from the interplay between the rods' intrinsic chiral rotation and their emergent cooperative dynamics. Notably, we observe a concurrent strengthening of the correlation between velocity components and azimuthal positions during vortex formation (see Supporting Information, Section S2). This correlation saturates upon reaching the steady vortex state, underscoring the system's transition to an ordered phase with well-defined collective motion. Our findings quantitatively reproduce key features of experimental vortex states reported in [4, 13, 28], thereby validating the CSPR model as an effective framework for studying the self-organization of chiral active matter [4, 13, 28].

3.1.2 Comparison of external and internal states of vortices

Recently, Xu et al. [28] experimentally demonstrated that bacterial swimmers exhibit significantly higher mean velocities of the vortex internal regions compared to those in the vortex external regions. Furthermore, their study revealed enhanced local

View Article Online
DOI: 10.1039/D5SM00380F

polar order in the vortex internal relative to the external regions. To quantitatively verify these observations in our system, we conducted comparative analyses of both mean velocity and local polarity between vortex internal and vortex external regions.

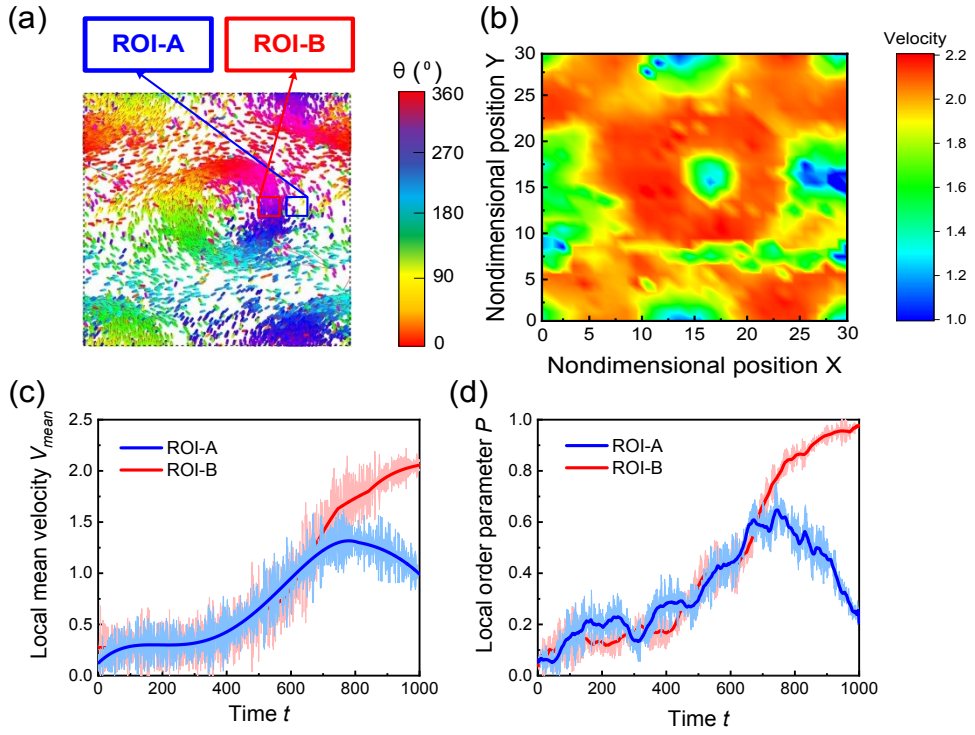

Fig. 3. Comparison of external and internal states of vortices. (a) The snapshots of a typical vortex ring, The blue boxes and red boxes represent the external and internal regions of the vortex, respectively, named as the square region of interest A (ROI-A) and the square region of interest B (ROI-B). (b) Velocity distribution heatmap of chiral self-propelled system at steady stage. (c) Variation of local mean velocity of the ROI-A and ROI-B of the stable vortex with respect to the simulation time *t*, respectively. (d) Variation of local order parameter of the ROI-A and ROI-B of the stable vortex with respect to the simulation time *t*, respectively.

To quantitatively compare local mean velocity and polarity between the external and internal vortex regions, we designated ROI-A (external) and ROI-B (internal) as representative sampling areas (blue box and red box in Figure. 3(a)). Figure 3(b) presents the velocity field distribution in the steady-state vortex, revealing significantly enhanced velocity magnitudes within the vortex ring compared to peripheral regions. Notably, spatial correlation analysis demonstrates colocalization of high-velocity and high-density regions (Supporting Information, Section S3), in excellent agreement with

View Article Online
DOI: 10.1039/D5SM00380F

experimental observations [4, 28]. We propose that this emergent velocity field arises from enhanced polar order within the vortex internal, which generates substantial local collective stress [48]. This stress field drives the accumulation of high-velocity chiral rods at the vortex ring, as evidenced by the temporal evolution of mean velocity and polarity in the chiral self-propelled system (Figures 3(c)-(d)). In addition, to verify the above results, we plotted the spatiotemporal variation heatmap of local mean velocity at different radial locations (Supporting Information, Section S4). Both quantities exhibit characteristic growth kinetics: initial stochastic fluctuations ($t < 300$) transition to monotonic increases ($300 < t < 800$), and reach steady-state stage ($t > 800$). This progression reflects the system's transition from disordered motion (where rod orientations and velocities are uncorrelated) to coordinated dynamics mediated by chiral interactions. This coordinate mechanism amplifies initial microscopic differences between rods through collective interactions, leading to macroscopic motion differentiation. Our findings demonstrate that vortex self-organization emerges from the synergistic coupling between local polar order and collective stress fields, reproducing key features of experimental chiral active matter systems [28].

3.2 Effects of aspect ratio

The aspect ratio, as an important geometric characteristic of active particles, plays a pivotal role in governing their self-organization behavior [54], collective alignment [55], and environmental interactions [56]. At the individual particle level, variations in the aspect ratio induce a morphological transition from isotropic spheres to anisotropic rods, consequently modulating interparticle forces, motility patterns, and emergent

View Article Online
DOI: 10.1039/D5SM00380F

collective behaviors. In most active matter systems, where particles interact via collision, attraction, or repulsion mechanisms, the aspect ratio critically determines both the nature and magnitude of these interactions.

3.2.1 Mean velocity and mean vorticity

Recently, Ilkanaiv et al. investigated length-dependent collective behaviors in swarming *Bacillus* subtilis variants through controlled experiments [57]. To examine the role of cellular aspect ratio in vortex-state dynamics, we conducted a series of simulations with precisely tuned bacterial aspect ratios spanning the range $a = 1 \sim 9$.

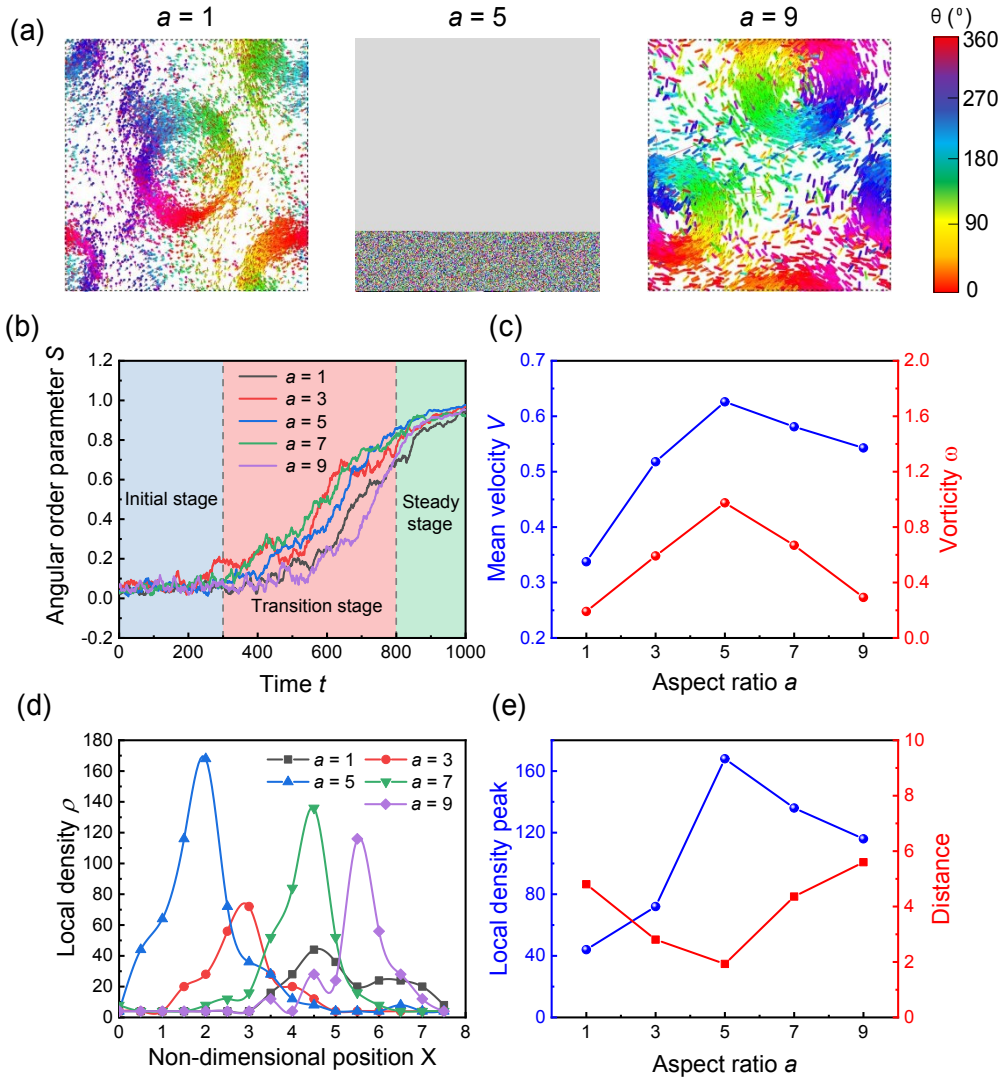

Fig. 4. Effects of different aspect ratios of micro-swimmers on chiral self-propelled system. (a)

Snapshots of chiral self-propelled rods under aspect ratio a = 1, a = 5 and a = 9, respectively. (b) Variation of the angular order parameter S of chiral self-propelled rod system with respect to the simulation time t under different aspect ratios. (c) The mean velocity and mean absolute vorticity as a function of aspect ratio. The nonmonotonic dependence, with a maximum at aspect ratio equal to 5. (d) The local density distribution of vortex state as a function of the Non-dimensional position X under aspect ratio a = 1, 3, 5, 7 and 9, respectively. (e) Local density peak and Distance with respect to the aspect ratio.

We first examine how aspect ratio affects the emergence pattern of a chiral self-propelled rod system. Figure 4(a) presents steady-state snapshots for various aspect ratios, demonstrating that stable vortex ring structures persist across the entire parameter range. Quantitative analysis of the angular order parameter S (Figure 4(b)) reveals three characteristic regimes: an initial disordered phase with low-magnitude fluctuations $(S \approx 0)$, a transitional growth phase exhibiting a linear increase in S, and a final ordered phase approaching complete alignment $(S \to 1)$. This universal progression suggests that while aspect ratio modulates local interactions, it does not fundamentally alter the pathway to vortex formation.

To establish a direct comparison with experimental observations [57], we quantitatively analyzed two key physical parameters: the mean velocity and vorticity of vortex states. Figure 4(c) presents the dependence of mean velocity and absolute vorticity on aspect ratio, revealing a striking non-monotonic relationship. Both mean velocity and absolute vorticity initially increase with aspect ratio, attaining maximum values at $a = 5$, followed by a gradual decrease at higher aspect ratios. This behavior shows excellent agreement with experimental measurements reported in Ref. [57]. We attribute this optimal aspect ratio phenomenon to competing mechanisms governing collective dynamics. On one hand, enhanced polar order within vortices generates stronger local active stresses [28], promoting coherent motion and transport in the

View Article Online
DOI: 10.1039/D5SM00380F

friction-dominated quasi-2D environment. This explains the initial positive correlation between aspect ratio and physical parameters. On the other hand, increasing the aspect ratio simultaneously amplifies interparticle repulsion due to greater excluded volume effects and increased potential energy between elongated rods. These repulsive interactions ultimately counteract the mobility enhancement, leading to the observed maximum at $a = 5$. The emergence of an optimal aspect ratio $(a = 5)$ suggests a delicate balance between two competing factors: the benefit of enhanced polar order for collective motion versus the detrimental effect of increased steric hindrance. These findings provide important insight into the design principles of chiral active matter systems, where geometric parameters can be easily tuned to maximize collective transport efficiency.

3.2.2 Local density of vortex state

In active matter systems, spatial density variations serve as fundamental drivers for diverse self-organization phenomena. Previous studies have demonstrated that particle aspect ratio can significantly affect both local density distributions and global packing fractions [56]. Building upon these findings, we examine the role of aspect ratio in modulating density distributions within vortex states, with a particular focus on vortex internal and vortex external regions.

As shown in Figure 4(d), we investigated the local density distribution ρ of the vortex state for different aspect ratios *a*. In order to clarify their intrinsic relationship, we quantitatively analyzed two key parameters from these distributions: the local density peak amplitude and its radial displacement from the vortex centroid (Figure

View Article Online
DOI: 10.1039/D5SM00380F

4(e)). Notably, the density peak amplitude follows a non-monotonic dependence on aspect ratio that mirrors the behavior observed for both velocity and vorticity (Figure 4(c)). As established in our earlier analysis, the self-enhanced mobility mechanism generates substantial local active stresses that promote higher mean velocities. A deeper examination of Figures 4(c)-(e) reveals a remarkable synchronization between velocity enhancement and density modulation. This coupled dynamics manifests through two key mechanisms: velocity-mediated recruitment of free chiral rods during vortex formation, and density-dependent modulation of velocity convergence. Specifically, increased local density facilitates more efficient momentum transfer through the collective, thereby amplifying mean velocities. Conversely, density reduction diminishes this velocity enhancement capability. These findings demonstrate a strong spatiotemporal coupling between velocity fields and density distributions in chiral active systems. The observed synchronization suggests that geometric parameters (aspect ratio) influence collective dynamics through their dual effects on both density distributions and active stress generation.

While variations in aspect ratio do not substantially alter the emergent vortex morphology, our analysis reveals a distinct non-monotonic dependence of the radial density peak position on aspect ratio (Figure 4(e)). Notably, this spatial dependence exhibits an inverse relationship with the trends observed for velocity, vorticity, and density amplitude. Specifically, the radial displacement of the density peak first decreases with the aspect ratio, reaches a minimum value at $a = 5$, and subsequently increases for larger aspect ratios. This non-monotonic behavior can be intuitively

View Article Online
DOI: 10.1039/D5SM00380F

explained by considering the competition between attraction effects by active stress–driven centripetal recruitment and repulsion effects by excluded volume interactions in the active system. As the aspect ratio increases, the average propulsion speed of the chiral rods also increases due to enhanced alignment, which amplifies the local active stress generated within the vortex. This active stress acts as a form of effective centripetal force, driving rods to circulate closer to the vortex centroid. This explains the initial negative correlation between the aspect ratio and the density peak distance. However, as the aspect ratio continues to increase, the chiral rods occupy more space and experience stronger excluded volume effects, resulting in increased short-range repulsive interactions. These interactions resist crowding and limit further inward aggregation, causing the high-density region to shift away from the vortex centroid at larger aspect ratios. Therefore, the observed spatial offset results from a balance between the active-stress-induced centripetal accumulation and the crowding-induced repulsion.

An interesting result is noteworthy that strong correlation among the mean velocity, vorticity, and local density. Local density may play a dominant role among these three physical parameters. During the dynamic evolution of active systems, significant differences of local density in different regions are inevitable. Compared to low-density regions, high-density regions typically exhibit stronger polarity due to their stronger coordination ability in the interaction between chiral self-propelled rods. Subsequently, local polarity plays a “bridge” role, indirectly connecting changes in local density with changes in mean velocity through the self-enhanced mobility

View Article Online
DOI: 10.1039/D5SM00380F

mechanism. In the self-enhanced mobility mechanism, the stronger the polarity of the local region around the chiral self-propelled rod, the greater the velocity of the chiral rods. Finally, we obtained the vorticity value by calculating the divergence of the velocity vector using formula $\omega = \nabla \times \mathbf{v}$, i.e., $\omega = \partial_x v_y - \partial_y v_x$.

3.3 Effect of self-enhanced mobility on vortex state

Experiments showed that the coupling relationship between polarity and velocity has direct a impact on the emergence behavior of dense suspensions [46, 47]. Inspired by the experimental results, the self-enhanced mobility mechanism further quantifies this relationship and vividly reflects it in the form of linear expression in the CSPR model. In this section, we pay attention to how the self-enhanced mobility mechanism modulates the collective dynamics in chiral self-propelled rod systems.

3.3.1 Chart of vortex emergence patterns

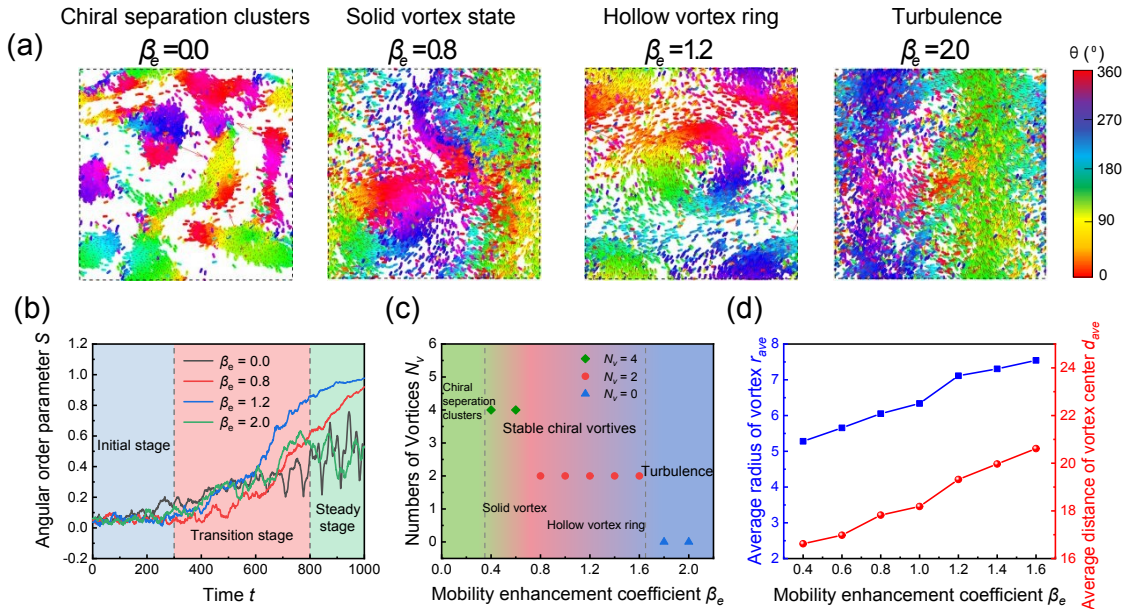

Fig. 5. Description of vortex emergence pattern of the chiral self-propelled system. (a) Snapshots of emergence pattern of chiral self-propelled rods under different mobility enhancement coefficients. (b) Variation of the angular order parameter S of chiral self-propelled rod system with respect to the simulation time t under different mobility enhancement coefficients. (c) Number of vortices in chiral self-propelled system with respect to mobility enhancement coefficient. (d) Variation of average radius

View Article Online
DOI: 10.1039/D5SM00380F

and average distance between vortices under different mobility enhancement coefficients.

As illustrated in Figure 5(a), we analyze the steady-state snapshots of CSPR systems under varying mobility enhancement coefficients $\beta_e = 0.0 - 2.0$. Our results reveal four distinct dynamical regimes: at weak coupling ($\beta_e = 0.0 - 0.2$), localized chiral separation clusters emerge within a disordered background, consistent with previous reports [58]; moderate coupling ($\beta_e = 0.4 - 0.8$) induces a transition to a well-ordered solid vortex state; stronger coupling ($\beta_e = 1.0 - 1.6$) drives a morphological transformation into hollow vortex rings; while ultra-strong coupling ($\beta_e > 1.6$) leads to fully developed turbulent disorder. For $\beta_e = 0.4 - 1.6$, S approaches close to 1 reflecting the structural stability of both solid and hollow vortex states, as shown in Figure 5(b). In contrast, extreme values of the mobility enhancement coefficient (either very low or very high) result in oscillatory and irregular characteristics of angular order parameter S during the steady stage, respectively. This is because chiral separation clusters have partial characteristics of vortex states, while disorder turbulent emergent states themselves are relatively complex and difficult to accurately characterize through angular order parameter S. Furthermore, we plotted the relationship between the mobility enhancement coefficient and the number of vortices, as shown in Figure 5(c). Interestingly, we found that in self-propelled systems, vortices always appear in pairs and in opposite directions. This is highly consistent with previous research findings [59]. In addition, we can intuitively observe that as the mobility enhancement coefficient increases, the number of vortices in the self-propelled system will disappear in pairs. The above results indicate that self-enhanced mobility significantly affects the emergence pattern of chiral

View Article Online
DOI: 10.1039/D5SM00380F

self-propelled rod systems, which are in good agreement with previous reports [28].

3.3.2 Characteristics of different vortex patterns

To reveal the pattern transition mechanism in chiral self-propelled rod systems, particularly between solid vortex and vortex ring configurations, we conducted a quantitative characterization of vortex morphology. By analyzing the average vortex radius and inter-vortex center distances across mobility enhancement coefficients ($\beta_e = 0.4 - 1.6$), we identify a clear monotonic increase in both parameters with a rising mobility enhancement coefficient β_e (Figure 5(d)). This trend, when correlated with the vortex number dependence shown in Figure 5(c), reveals a dual-phase regulatory mechanism: In the low mobility enhancement coefficient regime (structural dominance phase), increasing mobility enhancement primarily expands vortex dimensions, as evidenced by growing average radius. This expansion continues until geometric constraints of the finite system trigger a transition to the quantity adjustment phase, where vortex pairs annihilate to accommodate spatial limitations. Notably, this phase coincides with the morphological transition from solid vortices to hollow vortex rings. As the mobility enhancement coefficient further increases, the system re-enters a structure-dominated regime where continued vortex expansion becomes the primary response. Our findings demonstrate that self-enhanced mobility mediates pattern selection through an alternating sequence of structural and quantitative adaptations: first through dimensional scaling of individual vortices, then via collective number density adjustment, and finally through renewed structural modification. This hierarchical response mechanism explains the observed non-monotonic relationship

View Article Online
DOI: 10.1039/D5SM00380F

between α and vortex count while maintaining consistent radial expansion trends. The identified transition pathway suggests that pattern selection in active chiral systems represents a dynamic balance between intrinsic mobility-driven growth tendencies and extrinsic geometric constraints, with the crossover between structural and quantitative adaptation regimes governing emergent macroscopic patterns.

3.3.3 local density and vorticity of emergence patterns

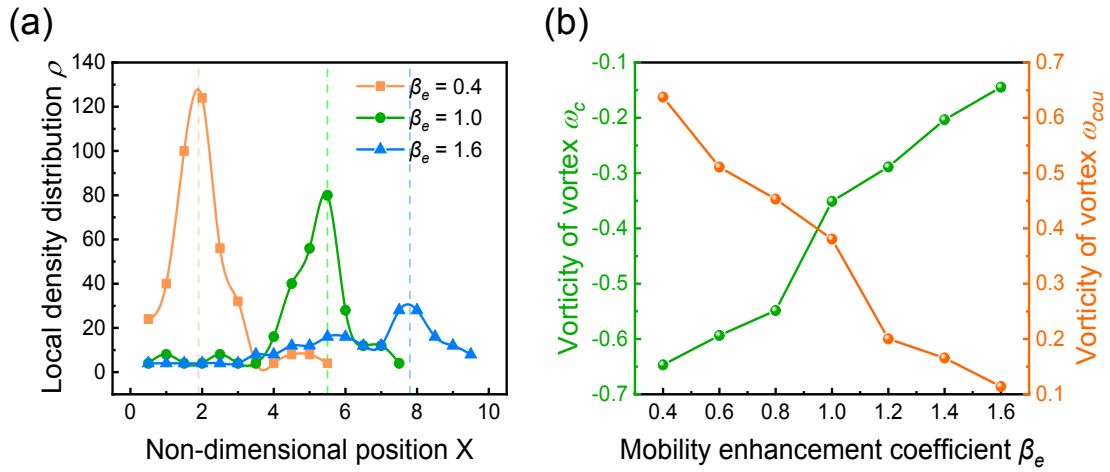

Fig. 6. Local density distribution and vorticity of vortex state. (a) Variation of local density distribution of the stable vortex at different dimensionless positions under different mobility enhancement coefficients. (b) Variation of vorticity of the stable vortex at different dimensionless positions under different mobility enhancement coefficients.

Next, we investigated the effect of the mobility enhancement coefficient on the local density and vorticity of vortex states. Figure 6(a) presents the evolution of local density as a function of dimensionless radial position for varying mobility enhancement coefficients β_e. We found that the peak local density exhibits a progressive reduction with increasing β_e, a direct consequence of vortex expansion under constant particle number conditions. This inverse relationship between vortex size and density concentration quantitatively confirms the structural scaling behavior identified in Figure 5(d). In addition, the radial position of density maxima shows a

View Article Online
DOI: 10.1039/D5SM00380F

consistent outward shift, providing independent verification of vortex expansion. It is interesting that with smaller mobility enhancement coefficient ($\beta_e = 0.4$), The local density peak at the non-dimensional position close to 0 (i.e. at the vortex centroid) is significantly higher than that at $\beta_e = 1.0$ and $\beta_e = 1.6$. This difference can also intuitively reflect the significant difference between the solid vortex and hollow vortex ring patterns at the vortex centroid. Complementary vorticity measurements (Figure 6(b)) reveal that the mean vorticity magnitude demonstrates monotonic attenuation with increasing β_e, suggesting reduced angular momentum density in larger vortices. The sign-conserved nature of vorticity (positive/negative values corresponding to counterclockwise/clockwise rotation respectively) confirms the preservation of chiral symmetry across all regimes. Our results establish that the mobility enhancement coefficient exerts multiscale control over vortex state characteristics, governing both structural and dynamical properties across different length scales. The observed density-velocity coupling suggests that self-enhanced mobility mediates energy redistribution within active chiral systems, with important implications for their transport properties and collective dynamics.

4 Discussion

To elucidate the fundamental mechanisms governing these intriguing self-organization phenomena in active matter systems, we typically employ intercorrelation analyses of key physical quantities. Building upon established methodologies [60], we investigate the system's collective dynamics through three fundamental correlation functions: (1) the velocity-velocity correlation function $C_{v,v}$,

View Article Online
DOI: 10.1039/D5SM00380F

which characterizes coordinated motion; (2) the angle-angle correlation function $C_{\theta,\theta}$, which quantifies orientational alignment; and (3) the position-position correlation function $C_{r,r}$, which reveals spatial ordering.

4.1 Velocity-velocity correlation function

The velocity-velocity correlation function serves as a fundamental quantitative descriptor for characterizing spatiotemporal coherence in active matter systems. In the context of chiral self-propelled rods, this correlation metric captures both the spatial extent and temporal persistence of directional alignment, thereby providing critical insights into the system's emergent collective dynamics and degree of orientational order. The mathematical formulation of this correlation function is given by:

$$C_{v,v}(t,\tau)=\left\langle \frac{1}{N}\sum_{\alpha}\mathbf{v}_{\alpha}(t).\mathbf{v}_{\alpha}(t-\tau)\right\rangle, \tag{16}$$

where τ denotes the lag time, $\mathbf{v}_{\alpha}(t)$ represents the unit vector of the spatial velocity of the α-th chiral self-propelled rod at time t; $\mathbf{v}_{\alpha}(t-\tau)$ is the unit velocity vector of the α-th chiral self-propelled rod at time t and lag time τ; And $C_{v,v}(t,\tau)$ represents the strength of the velocity-velocity correlation of the chiral self-propelled system at time t and lag time τ.

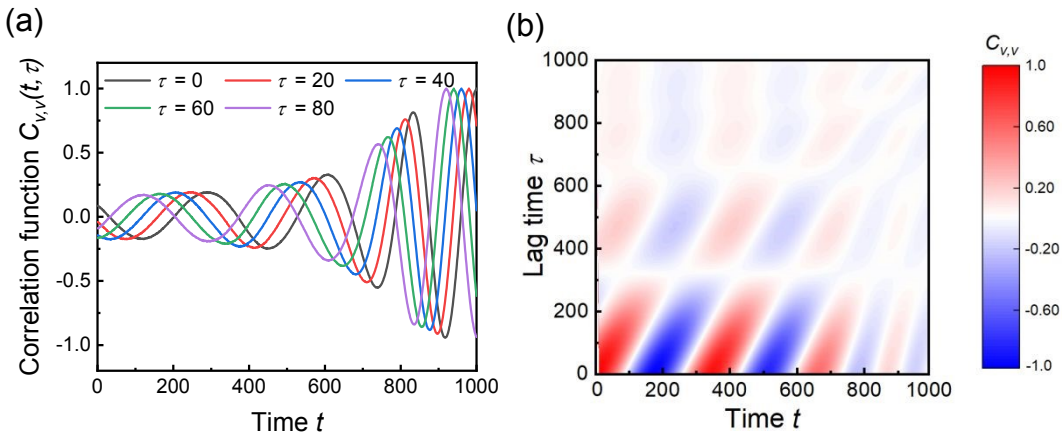

Fig. 7. Velocity-velocity correlation function of chiral self-propelled system. (a) Velocity-velocity correlation of a chiral self-propelled system with respect to time t under $\tau = 0$, $\tau = 20$, $\tau = 40$, $\tau = 60$ and $\tau = 80$. (b) Phase diagram of velocity-velocity correlation under different time t and lag time τ.

Figure 7(a) presents the temporal evolution of velocity-velocity correlation strength in the self-propelled rod system, revealing several key dynamical features. Notably, the correlation function exhibits sustained oscillations with increasing amplitude during vortex formation, indicating progressive enhancement of collective motion coherence. Quantitative analysis of correlation peaks reveals an increase in velocity correlation strength over time, exhibiting an inverse relationship with lag time τ, such that shorter delays correspond to stronger correlations. Remarkably, while the initial disordered and final steady-state phases show comparable correlation strengths across all lag times, the transitional regime displays markedly enhanced correlation dynamics. This suggests that the vortex formation process involves a distinct, temporally limited phase of intensified velocity field coupling. Subsequently, we constructed a phase diagram mapping the relationship between absolute time t and lag time τ, as presented in Figure 7(b). The results demonstrate that the velocity-velocity correlation exhibits joint dependence on both temporal parameters, manifesting as periodic oscillations. Two key findings emerge: first, reduced lag times correlate with enhanced velocity-velocity correlation strength in the vortex system; second, as the system approaches a stable ordered vortex state, the oscillation frequency of correlation intensity increases significantly.

4.2 Angle-angle correlation function

The angle-angle correlation function serves as a crucial analytical tool for

View Article Online
DOI: 10.1039/D5SM00380F

investigating the orientational ordering of rod-shaped particles in chiral active matter systems. This statistical measure quantitatively characterizes both spatial and temporal correlations in particle orientations, thereby providing essential insights into the emergence and evolution of directional order within such non-equilibrium systems.

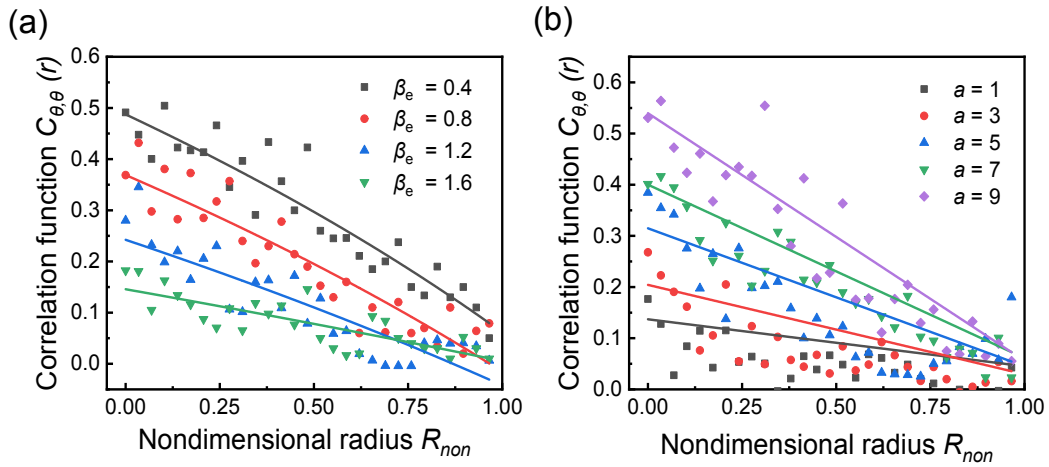

Fig. 8. Angle-angle correlation function of steady vortex state. (a) Angle-angle correlation function of steady vortex state under different mobility enhancement coefficients $\beta_e = 0.4$, $\beta_e = 0.8$, $\beta_e = 1.2$ and $\beta_e = 1.6$. (b) Angle-angle correlation function of steady vortex state under different aspect ratio $a = 1, 3, 5, 7,$ and 9.

Next, we utilized the angle-angle correlation function to study the steady vortex state, which takes the following form:

$$C_{\theta,\theta}(r) := \left\langle \frac{1}{N(N-1)} \sum_{\alpha,\beta} \mathbf{n}_\alpha \cdot \mathbf{n}_\beta \delta(r_{\alpha\beta} - r) \right\rangle, \tag{17}$$

where, r represents the dimensionless radius distance from the vortex centroid; $C_{\theta,\theta}(r)$ represents the angle-angle correlation at the dimensionless radius r; $\delta(r_{\alpha\beta} - r)$ denotes the Dirac δ-function selecting pairs of rods at a mutual distance r, $\mathbf{n}_\alpha = (\cos\theta_\alpha, \sin\theta_\alpha)$ is the orientation of the i-th chiral self-propelled rod; and $r_{\alpha\beta}$ is the distance between rod α and rod β and $\langle\cdot\rangle$ denotes the ensemble average. Figure 8 presents the angle-angle correlations in the steady vortex state under varying mobility enhancement coefficients β_e and aspect ratios a. As illustrated in Figure

View Article Online
DOI: 10.1039/D5SM00380F

8(a), the correlation strength $C_{\theta,\theta}$ exhibits a monotonic decrease with increasing mobility enhancement coefficient β_e, suggesting that higher mobility weakens orientational order. Conversely, Figure 8(b) reveals that $C_{\theta,\theta}$ increases with aspect ratio *a*, indicating enhanced alignment in more anisotropic rods. Moreover, regardless of mobility enhancement coefficient β_e or aspect ratio *a*, $C_{\theta,\theta}$ decays with r, demonstrating a progressive loss of orientational coherence from the vortex centroid to its periphery. This radial dependence implies that alignment interactions are strongest near the vortex centroid and diminish toward the edge.

4.3 Position-position correlation function

The position-position correlation function is an important tool for studying the spatial distribution and motion patterns in a chiral self-propelled system. It is used to describe the spatial correlation of rod positions, reflecting the structural order, aggregation behavior, and dynamic characteristics of the chiral self-propelled system.

Finally, we utilized the position-position correlation function to study the spatial distribution of vortices, which takes the following form:

$$C_{x,x}(r) = g(r) := \left\langle \frac{1}{N(N-1)} \sum_{\alpha,\beta} \delta\left(r - r_{\alpha\beta}\right) \right\rangle, \tag{18}$$

where $C_{x,x}(r)$ represents the position-position correlation at the distance *R*; $\delta\left(r_{\alpha\beta} - r\right)$ denotes the Dirac δ-function selecting pairs of rods at amutual distance *r*; $r_{\alpha\beta}$ is the distance between rod α and rod β and $\langle\cdot\rangle$ denotes the ensemble average.

View Article Online
DOI: 10.1039/D5SM00380F

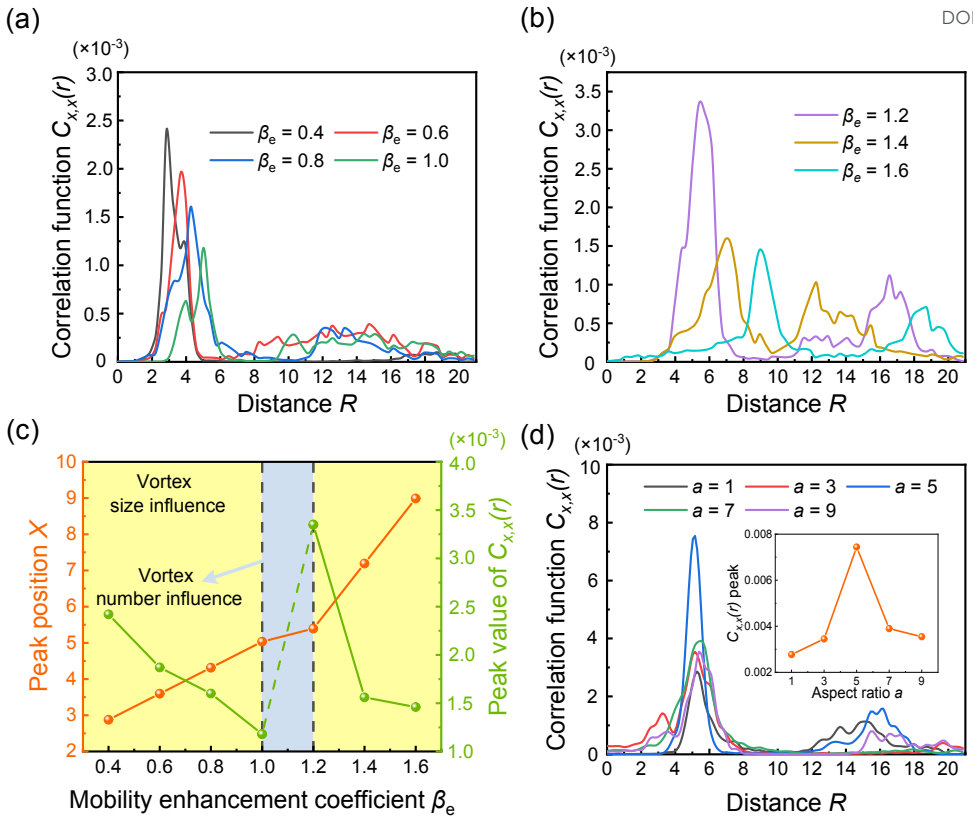

Fig. 9. Position-position correlation function of steady vortex state. (a) Position-position correlation function of solid vortex state under different mobility enhancement coefficients $\beta_e = 0.4$, $\beta_e = 0.6$, $\beta_e = 0.8$ and $\beta_e = 1.0$. (b) Position-position correlation function of hollow vortex ring under different mobility enhancement coefficients $\beta_e = 1.2$, $\beta_e = 1.4$ and $\beta_e = 1.6$. (c) The distance R and the peak value of steady vortex state under different mobility enhancement coefficients. (d) Position-position correlation function of steady vortex state under different aspect ratios $a = 1, 3, 5, 7,$ and 9. Peak value of position-position function correlation strength under different aspect ratios (inset).

Figure 9 presents the position-position correlation profiles for the vortex system under varying mobility enhancement coefficients β_e and aspect ratios a. Figures 9(a) and 9(b) contrast the position-position correlation functions $C_{x,x}$ for solid vortex and hollow vortex ring states, respectively. Notably, the solid vortex pattern exhibits a characteristic single-peak characteristic, while the hollow vortex ring displays a distinct double-peak signature. The characteristic differences stem from fundamental differences in vortex organization, with the solid vortex state exhibiting multiple randomly distributed vortices in contrast to the hollow vortex ring configuration's

View Article Online
DOI: 10.1039/D5SM00380F

characteristic single vortex pair. The single-peak profile emerges from spatial averaging effects, where the random distribution and mutual annihilation of numerous vortices suppress secondary correlation features. Conversely, the well-defined double-peak structure in hollow vortex rings reflects the concentrated spatial arrangement of the vortex pair. Figure 9(c) presents the quantitative analysis showing that as the mobility enhancement coefficient β_e increases, two distinct trends emerge: a decrease in peak correlation strength accompanied by a proportional increase in the characteristic length scale R. These trends primarily reflect vortex expansion driven by enhanced mobility. However, we observe discontinuous jumps in the position-position correlation strength (Figure. 9(c)), attributable to a paired reductions in vortex number that permit subsequent expansion, consistent with our earlier findings. Figure 9(d) examines aspect ratio effects, showing a non-monotonic variation in peak correlation strength without significant changes in R. This confirms that aspect ratio a primarily affects local packing rather than global vortex organization, as previously established. Collectively, these results demonstrate that position correlations directly reflect the local density distribution in chiral active matter, providing a sensitive probe for vortex dynamics and pattern formation.

5 Conclusions

In summary, we have developed an extended chiral self-propelled rod model with incorporating self-enhanced mobility, which enriches the theoretical framework for active matter systems. Our model not only reproduces experimentally observed vortex structures, but also elucidates the physical mechanisms underlying their emergence. It

View Article Online
DOI: 10.1039/D5SM00380F

highlights how polarity–mobility feedback, repulsion–alignment interplay, and aspect ratio-driven packing effects jointly regulate large-scale self-organization behavior. These findings provide theoretical insights that help interpret experimental patterns and inform the design of synthetic active systems. Specifically, our simulations have successfully characterized the formation dynamics of spontaneous vortices, the distinct structural differences between internal and external vortex states, and the pivotal roles of rod aspect ratio and self-enhanced mobility in governing vortex pattern formation and transitions. Key findings reveal that while aspect ratio variations primarily modulate vortex properties (including mean velocity profiles, vorticity distributions, and local density variations), they do not directly drive pattern transitions. Crucially, the self-enhanced mobility mechanism serves dual functions: stabilizing vortex states and enabling controlled pattern transitions through regulation of vortex size and number. Our multi-faceted analysis employing velocity, angular, and positional correlation functions has provided complementary perspectives on these collective phenomena. These results establish a fundamental understanding of how morphological parameters and physical interactions synergistically govern emergent behaviors in active systems, offering novel insights into spontaneous vortex self-organization.

To date, it has been challenging to quantitatively compare with the experimental results of dense active suspension. This may be related to the inherent limitation that our model is purely physical model. However, we provide a paradigm for how to extract key physical mechanisms from interesting experimental phenomena to expand

View Article Online
DOI: 10.1039/D5SM00380F

the existing model. With the help of other vital experiments of dense active suspensions, such as the regulation of hydrodynamic and chemical signals on the active system, we can further test and expand our model from the intricate interplay of multiple factors. In addition, the CSPR model developed here suggests promising strategies for manipulating collective states in engineered active systems, with potential applications spanning from nanorobotic swarms to programmable active metamaterials. Future work will incorporate additional physical factors including hydrodynamic interactions, mechanotaxis, and chemotactic responses to develop a more complete theoretical description of vortex dynamics in active matter.

Author contributions

Shuang-Quan He: Software, Validation, Formal analysis, Investigation, Data curation, Writing original draft, Visualization. **Zhuo Chang:** Conceptualization, Formal analysis, Writing original draft, Writing review & editing. **Dong Liang:** Formal analysis, Investigation, Data curation. **Chen-He Li:** Formal analysis, Investigation. **Qian-lei Liang:** Conceptualization, Formal analysis, Resources, Writing original draft. **Xu Yin:** Conceptualization, Formal analysis, Writing original draft, Writing- review & editing. **Guang-Kui Xu:** Conceptualization, Methodology, Formal analysis, Resources, Data curation, Writing original draft, Writing-review & editing, Visualization, Project administration, Funding acquisition.

View Article Online
DOI: 10.1039/D5SM00380F

Data availability

The data supporting this study are available within the article.

Conflicts of Interest

The authors declare that there are no conflicts of interest associated with the present study.

Acknowledgements

Supports from the National Natural Science Foundation of China (No.12072252,), the Nature Science Basic Research Plan in Shaanxi Province of China (No.2025JC-QYCX-001), and the Fundamental Research Funds for the Central Universities of China are gratefully acknowledged.

View Article Online
DOI: 10.1039/D5SM00380F

References

1. S. Ramaswamy, *Journal of Statistical Mechanics: Theory and Experiment*, 2017, **2017,** 054002.
2. H. Xu, Y. Huang, R. Zhang and Y. Wu, *Nature Physics*, 2023, **19**, 46-51.
3. K. Beppu, Z. Izri, J. Gohya, K. Eto, M. Ichikawa and Y. T. Maeda, *Soft Matter*, 2017, **13**, 5038-5043.
4. S. Liu, S. Shankar, M. C. Marchetti and Y. Wu, *Nature*, 2021, **590**, 80-84.
5. H. H. Wensink, J. Dunkel, S. Heidenreich, K. Drescher, R. E. Goldstein, H. Löwen and J. M. Yeomans, *Proceedings of the National Academy of Sciences of the United States of America*, 2012, **109**, 14308-14313.
6. J. Dunkel, S. Heidenreich, K. Drescher, H. H. Wensink, M. Baer and R. E. Goldstein, *Physical Review Letters*, 2013, **110**, 228102.
7. A. Doostmohammadi, M. F. Adamer, S. P. Thampi and J. M. Yeomans, *Nature Communications*, 2016, **7**, 10557.
8. M. M. Genkin, A. Sokolov, O. D. Lavrentovich and I. S. Aranson, *Physical Review X*, 2017, **7**, 011029.
9. M. E. Cates and J. Tailleur, *Annual Review of Condensed Matter Physics*, 2015, **6**, 219-244.
10. G. Gonnella, D. Marenduzzo, A. Suma and A. Tiribocchi, *Comptes Rendus Physique*, 2015, **16**, 316-331.
11. L. Caprini and H. Löwen, *Physical Review Letters*, 2023, **130**, 148202.
12. I. H. Riedel, K. Kruse and J. Howard, *Science*, 2005, **309**, 300-303.
13. Y. Sumino, K. H. Nagai, Y. Shitaka, D. Tanaka, K. Yoshikawa, H. Chate and K. Oiwa, *Nature*, 2012, **483**, 448-452.
14. Y. Katz, K. Tunstrom, C. C. Ioannou, C. Huepe and I. D. Couzin, *Proceedings of the National Academy of Sciences of the United States of America*, 2011, **108**, 18720-18725.
15. A. Cavagna, I. Giardina and T. S. Grigera, *Physics Reports: Review Section of Physics Letters*, 2018, **728**, 1-62.
16. M. Yanai, *Reviews of Geophysics*, 1964, **2**, 367-414.
17. S. R. K. Vedula, A. Ravasio, C. T. Lim and B. Ladoux, *Physiology*, 2013, **28**, 370-379.
18. A. Ziepke, I. Maryshev, I. S. Aranson and E. Frey, *Nature Communications*, 2022,

View Article Online
DOI: 10.1039/D5SM00380F

13, 6727.

19. W. M. Durham, E. Climent, M. Barry, F. De Lillo, G. Boffetta, M. Cencini and R. Stocker, *Nature Communications*, 2013, **4**, 2148.
20. D. Needleman and Z. Dogic, *Nature Reviews Materials*, 2017, **2**, 17048.
21. R. Zhang, A. Mozaffari and J. J. de Pablo, *Nature Reviews Materials*, 2021, **6**, 437-453.
22. F. Ji, Y. Wu, M. Pumera and L. Zhang, *Advanced Materials*, 2023, **35**, 2203959.
23. P. Patra, K. Beyer, A. Jaiswal, A. Battista, K. Rohr, F. Frischknecht and U. S. Schwarz, *Nature Physics*, 2022, **18**, 586-594.
24. D. Nakane, S. Odaka, K. Suzuki and T. Nishizaka, *Journal of Bacteriology*, 2021, **203**, e00073-00021.
25. H. Wioland, F. G. Woodhouse, J. Dunkel, J. O. Kessler and R. E. Goldstein, *Physical Review Letters*, 2013, **110**, 268102.
26. E. Lushi, H. Wioland and R. E. Goldstein, *Proceedings of the National Academy of Sciences of the United States of America*, 2014, **111**, 9733-9738.
27. K. Suzuki, M. Miyazaki, J. Takagi, T. Itabashi and S. i. Ishiwata, *Proceedings of the National Academy of Sciences of the United States of America*, 2017, **114**, 2922-2927.
28. H. Xu and Y. Wu, *Nature*, 2024, **627**, 553-558.
29. T. Vicsek, A. Czirok, E. Benjacob, I. Cohen and O. Shochet, *Physical Review Letters*, 1995, **75**, 1226-1229.
30. M. Meschede and O. Hallatschek, *New Journal of Physics*, 2013, **15**, 045027.
31. F. Ginelli, *European Physical Journal-Special Topics*, 2016, **225**, 2099-2117.
32. A. Costanzo and C. K. Hernelrijk, *Journal of Physics D-Applied Physics*, 2018, **51**, 134004.
33. A. Wysocki, R. G. Winkler and G. Gompper, *Epl*, 2014, **105**, 48004.
34. A. P. Solon, M. E. Cates and J. Tailleur, *European Physical Journal-Special Topics*, 2015, **224**, 1231-1262.
35. F. Peruani, *European Physical Journal-Special Topics*, 2016, **225**, 2301-2317.
36. S. R. McCandlish, A. Baskaran and M. F. Hagan, *Soft Matter*, 2012, **8**, 2527-2534.
37. S. Weitz, A. Deutsch and F. Peruani, *Physical Review E*, 2015, **92**, 012322.
38. O. Duman, R. E. Isele-Holder, J. Elgeti and G. Gompper, *Soft Matter*, 2018, **14**, 4483-4494.
39. M. Baer, R. Grossmann, S. Heidenreich and F. Peruani, *Annual Review of*

View Article Online
DOI: 10.1039/D5SM00380F

Condensed Matter Physics, 2020, **11**, 441-466.

40. Y. Liu, Y. Yang, B. Li and X. Q. Feng, *Soft Matter*, 2019, **15**, 2999-3007.
41. O. J. Meacock, A. Doostmohammadi, K. R. Foster, J. M. Yeomans and W. M. Durham, *Nature Physics*, 2021, **17**, 205-210.
42. X. Q. Shi and Y. Q. Ma, *Nature Communications*, 2013, **4**, 3013.
43. T. Kirchhoff, H. Löwen and R. Klein, *Physical Review E*, 1996, **53**, 5011-5022.
44. H. H. Wensink and H. Löwen, *Journal of Physics: Condensed Matter*, 2012, **24**, 464130.
45. J. Yan, M. Han, J. Zhang, C. Xu, E. Luijten and S. Granick, *Nature Materials*, 2016, **15**, 1095-1099.
46. L. H. Cisneros, R. Cortez, C. Dombrowski, R. E. Goldstein and J. O. Kessler, *Experiments in Fluids*, 2007, **43**, 737-753.
47. L. H. Cisneros, J. O. Kessler, S. Ganguly and R. E. Goldstein, *Physical Review E*, 2011, **83**, 061907.
48. S. Ramaswamy, *Annual Review of Condensed Matter Physics*, 2010, **1**, 323-345.
49. S. Q. He, X. Yin, D. Liang, Z. Chang and G. K. Xu, *Physical Review E*, 2025, **111**, 014411.
50. C. Chen, S. Liu, X. Q. Shi, H. Chate and Y. Wu, *Nature*, 2017, **542**, 210-214.
51. A. Be′er and G. Ariel, *Movement Ecology*, 2019, **7**, 9.
52. K. P. O'Keeffe, H. Hong and S. H. Strogatz, *Nature Communications*, 2017, **8**, 1504.
53. M. Riedl, I. Mayer, J. Merrin, M. Sixt and B. Hof, *Nature Communications*, 2023, **14**, 5633.
54. A. Be′er, B. Ilkanaiv, R. Gross, D. B. Kearns, S. Heidenreich, M. Baer and G. Ariel, *Communications Physics*, 2020, **3**, 66.
55. P. Bera, A. Wasim, J. Mondal and P. Ghosh, *Soft Matter*, 2021, **17**, 7322-7331.
56. M. Theers, E. Westphal, K. Qi, R. G. Winkler and G. Gompper, *Soft Matter*, 2018, **14**, 8590-8603.
57. B. Ilkanaiv, D. B. Kearns, G. Ariel and A. Be′er, *Physical Review Letters*, 2017, **118**, 158002.
58. L. A. Hoffmann and L. Giomi, *Physical Review E*, 2025, **111**, 015427.
59. K. Han, G. Kokot, O. Tovkach, A. Glatz, I. S. Aranson and A. Snezhko, *Proceedings of the National Academy of Sciences of the United States of America*, 2020, **117**, 9706-9711.

60. S. Ceron, K. O'Keeffe and K. Petersen, *Nature Communications*, 2023, **14**, 940. View Article Online
DOI: 10.1039/D5SM00380F

View Article Online
DOI: 10.1039/D5SM00380F

Data Availability

The data supporting this study are available within the article.